Bio-Design and Manufacturing (2025) 8:344–358
https://doi.org/10.1631/bdm.2400313

RESEARCH ARTICLE

# $Mg^{2+}$-containing composite scaffolds mediate macrophage polarization to enhance meniscus regeneration

Zong Li[1,2,3] · Weili Shi[1,2,3] · Ming Tian[4] · Wenqiang Yan[1,2,3] · Yifei Fan[1,2,3] · Jin Cheng[1,2,3] · Xiaoqing Hu[1,2,3] · Xi Gong[1,2,3] · Yingfang Ao[1,2,3]

Received: 7 August 2024 / Accepted: 15 September 2024


## Abstract

Meniscal injury, a prevalent and challenging medical condition, is characterized by poor self-healing potential and a complex microenvironment. Tissue engineering scaffolds, particularly those made of silk fibroin (SF)/hyaluronic acid methacryloyl (HAMA) and encapsulating $Mg^{2+}$, are promising options for meniscal repair. However, the inflammatory response following implantation is a significant concern. In this study, we prepared a composite SF/HAMA-Mg hydrogel scaffold, evaluated its physical and chemical properties, and detected its fibrochondrogenic differentiation effect in vitro and the healing effect in a rabbit meniscus defect model in vivo. Our results showed that the scaffold differentiates pro-inflammatory M1 macrophages into anti-inflammatory M2 macrophages after implantation, thereby reducing inflammation and facilitating the growth and repair of meniscus tissue. Further, the composite scaffold provided a conducive milieu for cell proliferation, anticipatory differentiation, and generation of extracellular matrix. In summary, composite SF/HAMA-Mg scaffolds exhibit exceptional biocompatibility and anti-inflammatory properties, demonstrating superior potential for meniscal repair.

## Graphical abstract

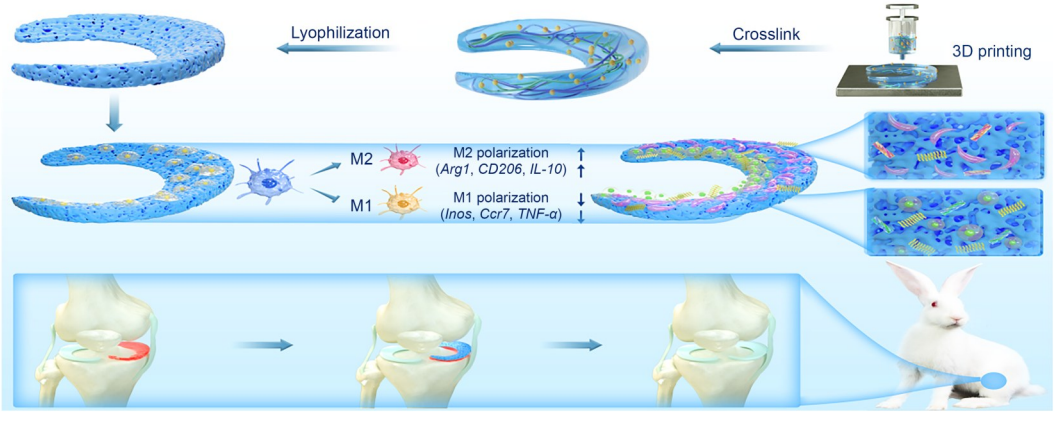


**Keywords** Meniscal repair · Magnesium · Macrophage polarization · Multifunctional composite hydrogel

Zong Li, Weili Shi, and Ming Tian have contributed equally to this work.

✉ Xi Gong
Gongxibjmu@sina.com

✉ Yingfang Ao
aoyingfang@163.com

[1] Department of Sports Medicine, Peking University Third Hospital, Institute of Sports Medicine of Peking University, Beijing 100191, China

[2] Beijing Key Laboratory of Sports Injuries, Beijing 100191, China

[3] Engineering Research Center of Sports Trauma Treatment Technology and Devices, Ministry of Education, Beijing 100191, China

[4] Civil Aviation General Hospital, Beijing 100123, China

## 1 Introduction

The meniscus, an anisotropic tissue within the knee joint, significantly influences stress distribution, lubrication, and joint stability [1, 2]. A meniscus lesion compromises the positive impact of this tissue, leading to joint instability and subsequent cartilage degeneration, potentially culminating in osteoarthritis [3, 4]. In addition, the poor vascularity of the medial part of the meniscus often inhibits intrinsic recovery [5, 6]. Therefore, it is necessary to effectively reinstate the functionality of joints and hinder further degeneration by employing a tissue with suitable structure, composition, and mechanical characteristics for rectifying impairments in the meniscus. Bioinspired gradient scaffolds for meniscus and osteochondral tissue engineering have been developed by simulating gradient characteristics, such as the pores, components, and target-inducing factors, in heterogeneous tissues to recreate the anisotropic features of meniscus and osteochondral matrices [7–9]. However, despite numerous attempts to address this issue, current treatment options have been largely inadequate in regenerating a functional meniscus comparable to the native one [10–13].

Recently, natural hydrogels have emerged as promising candidates for treating meniscal injuries [14–17] largely due to their easy formulation, precision in targeted injection, and excellent biodegradability and biocompatibility. Despite their prevalence, natural hydrogels often exhibit insufficient mechanical properties and a propensity for rapid degradation within the body. To address these deficiencies, various cross-linking techniques, including physical and chemical methods, can be employed to fortify the polymer network and enhance the physical characteristics of hydrogels [18–20]. Photopolymerization has emerged as a significant area of research in the synthesis of hydrogels, primarily owing to merits [21–24], including the ability to operate at low reaction temperatures, rapid solidification, a straightforward and gentle preparation process, cost-effectiveness, and the elimination of the need for organic solvents [25, 26].

Hyaluronic acid is the fundamental constituent of the extracellular matrix within joint fluids, boasting excellent biocompatibility and biodegradability, thereby making it highly advantageous for medical applications [27–30]. Notably, a hyaluronic acid methacryloyl (HAMA) hydrogel has garnered significant interest due to its minimal immunogenicity and biological activity [31–33], and has potential applicability to the treatment of meniscal injuries. However, photocured HAMA gels typically exhibit poor mechanical properties and rapid degradation, which compromises their capacity to withstand external forces, thereby increasing the risk of rupture. Thus, there is an urgent need to develop HAMA-based composite hydrogels that improve on this factor.

Silk fibroin (SF), a naturally occurring fibrous protein derived from the cocoons of domestic silkworms, has been extensively used in the development of hydrogels due to its distinctive mechanical properties, high biocompatibility, and controlled biodegradation rate [34–37]. The incorporation of SF into HAMA hydrogels enables the replication of extracellular matrix (ECM) composition and structure, resulting in enhanced strength and regulated hydrogel degradation.

For developing medical implants, it is critical to regulate the immune response to biomaterials implanted in vivo. Engineered biomaterials that stimulate macrophage behavior are essential for promoting tissue regeneration, as an increase in M2-like macrophages can be beneficial for enhancing tissue repair and healing. Magnesium is a vital component in the human body, being involved in multiple physiological processes, including immunomodulation [38–40]. In tissue regeneration research, hydrogels incorporating $Mg^{2+}$ recently garnered considerable interest owing to their remarkable biocompatibility and modifiability. Further, hydrogels supplemented with $Mg^{2+}$ can enhance cell adhesion, proliferation, differentiation, ECM secretion, and immune response modulation [41]. In this study, $Mg^{2+}$ was incorporated into SF/HAMA hydrogels to facilitate tissue regeneration by releasing $Mg^{2+}$ gradually during scaffold degradation and to investigate the regulatory impact of $Mg^{2+}$ on synovium-derived mesenchymal stem cells (SMSCs) and macrophages. Furthermore, the composite SF/HAMA-Mg hydrogel was surgically implanted into a medial meniscus defect in a rabbit model to evaluate its functional effects (Fig. 1). The underlying hypothesis is that this cell-free SF/HAMA-Mg hydrogel could enhance meniscus regeneration by promoting a macrophage shift from M1 to M2.

## 2 Materials and methods

### 2.1 Scaffold fabrication

Hyaluronic acid, trypsin, pepsin, Trixon X-100, methacrylic anhydride, and lithium phenyl-2,4,6-trimethylbenzoylphosphinate were purchased from Sigma-Aldrich (Beijing, China). Cocoons were purchased from a cocoon base (Guangdong Cocoon Base, China). Magnesium chloride was purchased from Solarbio (Beijing, China).

Preparation of the SF/HAMA-Mg hydrogel: SF was prepared as previously described [42]. SF purification involved the removal of sericin, a protein with adhesive properties, from the cocoons by immersing them in a boiling 0.02 mol/L sodium carbonate solution for 1 h. Next, the cocoons were rinsed with distilled water to completely eliminate the degumming solution. The purified SF was then dissolved in a solution of lithium bromide (9.3 mol/L), for 1 h at 70 °C. The resulting solution was subjected to dialysis in distilled

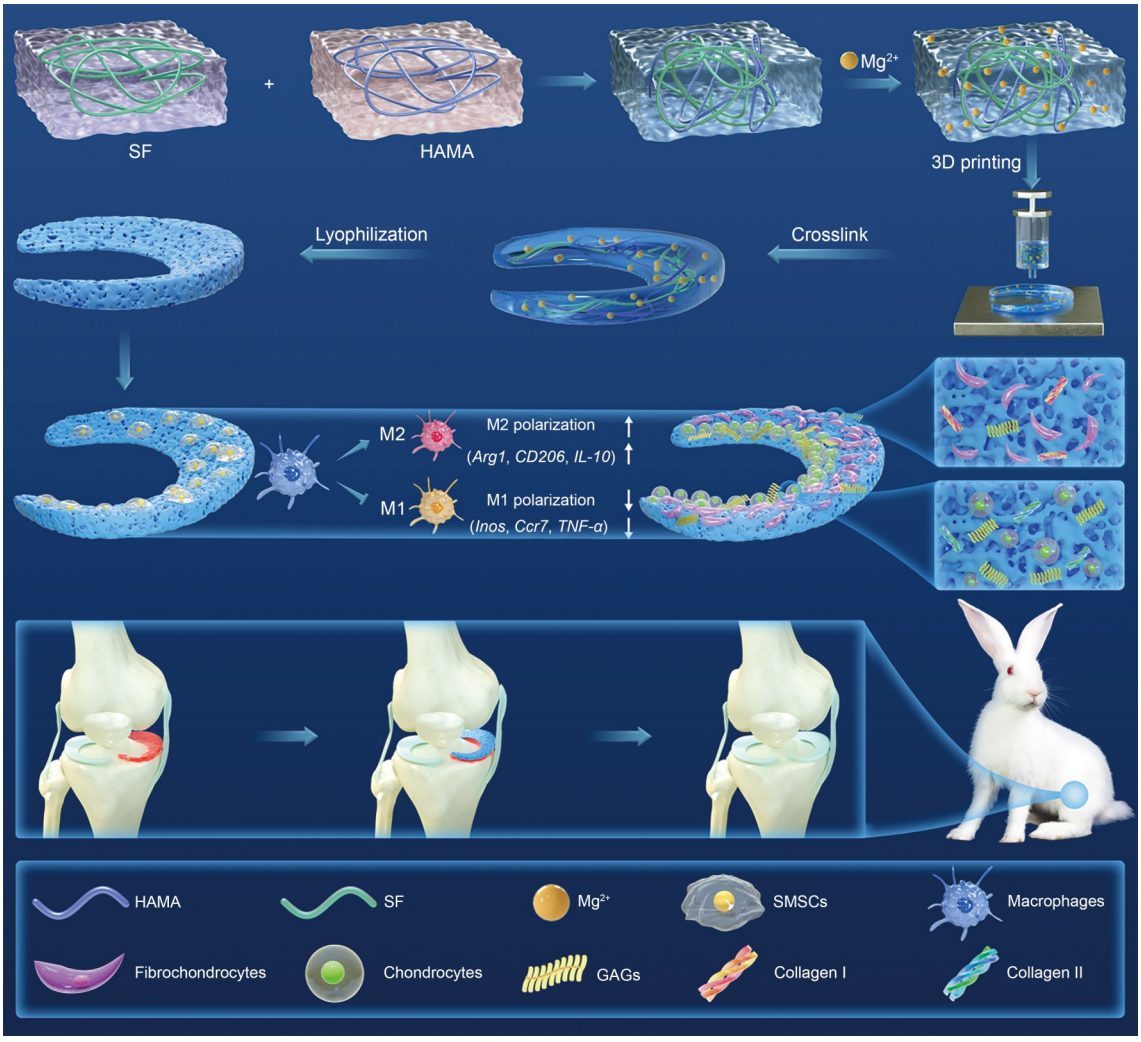


**Fig. 1** Schematic illustration of the use of an SF/HAMA-Mg hydrogel in meniscus regeneration. GAG: glycosaminoglycan

water for 48 h, using benzoylated dialysis tubing with a molecular weight cut-off (MWCO) of 2 kDa. To concentrate the SF, it was exposed to a 20% (mass fraction) poly(ethylene glycol) solution for ⩾6 h. The SF concentration was determined by weighing the dry weight of the SF solution after placing it in an oven at 70 °C overnight. Additionally, the prepared SF solution was stored at 4 °C until ready for use. In this study, a total volume of 500 mL of deionized water was utilized to dissolve 5 g of hyaluronic acid with a molecular weight of 1400 kDa. Dissolution was achieved through vigorous stirring. Subsequently, a dropwise addition of 20 mL of methacrylic anhydride was performed in an ice bath. The pH of the solution was maintained between 8 and 11, and adjustments were made using a 5 mol/L NaOH solution. The reaction was carried out overnight in darkness at 0 to 4 °C. Once the reaction was complete, the solution underwent centrifugation at 5000 r/min to eliminate any insoluble components. The pH of the solution was then adjusted to 7.4 by adding a 1 mol/L HCl solution. The resulting compound was subsequently frozen and subjected to lyophilization after three days of dialysis against deionized water. In our study, the hydrogel was formulated using a combination of 10% SF, 2% HAMA, 0.12% magnesium chloride ($MgCl_2$), and 0.1% (1 mg/mL) lysine amino peptidase.

To replicate the natural structure of the medial meniscus, a three-dimensional (3D) computer-aided design model was developed. This model integrated collagen fibers aligned in both circumferential and radial orientations, resembling the organization in the native meniscus. To this end, a wedge-shaped arc disk was designed to imitate the meniscus. Hydrogel application was meticulously performed layer by layer, following a predetermined plan, using a 3D-Bioplotter (Envision TEC 4th generation; Gladbeck, Germany). During printing, blue light (405 nm) was employed on the receiving platform to photocrosslink the printed hydrogel. Subsequently, the scaffolds were further crosslinked in ethanol and then lyophilized until further use.

## 2.2 Rheological measurement

The hydrogel's rheological characteristics were analyzed using a rheometer (ARES-G2, TA Instruments, USA). The viscoelastic behavior was assessed across the angular frequency spectrum of $10^{-1}$–$10^{2}$ Hz. The shear viscosity was measured across from $10^{-2}$ to $10^{2}$ shear rates.

## 2.3 Fourier transform infrared spectroscopy

An Affinity-1S Fourier transform infrared (FTIR) spectrometer was utilized to conduct attenuated total reflection FTIR spectroscopy on hydrogels comprising SF, SF/HAMA, and SF/HAMA/$Mg^{2+}$. The spectral analysis was performed within the scanning range of 400 to 4000 $cm^{-1}$, at a resolution of 4 $cm^{-1}$.

## 2.4 Scanning electron microscopy (SEM)

The scaffolds were immobilized with a 2.5% (volume fraction) solution of glutaraldehyde, subjected to dehydration using a graded ethanol series and dried utilizing $CO_2$ (EM CPD300; Leica, Wentzler, Germany), followed by gold sputtering. The scaffold microstructure was examined using an SEM model S-4800 with field emission technology from Hitachi (Tokyo, Japan).

## 2.5 Biomechanical testing

Different-sized scaffold samples were prepared to conduct biomechanical testing using an AGS-X Precision Universal Tester (Shimadzu, Japan). The samples were kept moist with phosphate-buffered saline (PBS) during the entire testing process. The unconfined compressive strength was assessed using 15 mm×15 mm×15 mm cubes, while the tensile strength was evaluated using 5 mm×5 mm×15 mm specimens.

## 2.6 Degradation rate

The scaffolds were submerged in PBS (pH=7.4) and an XIV protease solution at 0.5 U/mL and 37 °C. At the corresponding time points, the scaffolds were accurately weighed ($W_t$). The initial scaffold weight was $W_0$.

$$\text{Degradation ratio}=(W_0-W_t)/W_0\times 100\%.$$

## 2.7 Swelling test

Swelling tests were conducted to determine the swelling properties of the samples. Freeze-dried samples were submerged in PBS (pH=7.4) at 37 °C for 24 h. Next, any excess water was eliminated, and the samples were weighed. The equilibrated swelling ratio (ESR) was calculated as follows:

$$\text{ESR}=(W_s-W_d)/W_d\times 100\%,$$

where $W_s$ and $W_d$ represent the hydrogel weight in the swollen and dry states, respectively.

## 2.8 $Mg^{2+}$ release

To measure the concentration of released $Mg^{2+}$, the scaffolds were submerged in PBS for 20 d. Ion concentration measurements were carried out using ICP-OES (Optima 7000 DV, PerkinElmer, USA) and ICP-MS (ICP Q, Thermo Scientific, USA).

## 2.9 SMSC culture and identification

The methods for isolating and culturing SMSCs were as previously described [43]. Sprague–Dawley rats weighing 80 g were selected, and synovial tissue was collected from the suprapatellar bursa. The synovium was then digested with 0.2% type I collagenase (Invitrogen, Carlsbad, CA, USA) in alpha-minimum essential medium (α-MEM) for 30 min at 37 °C. Then, SMSCs collected by centrifugation were incubated in a complete medium, which was changed every three days. SMSCs were evaluated for specific cell surface antigen labeling by flow cytometry. Positive markers included CD44 (ab112179) and CD90 (ab225), and negative markers included CD34 (ab187284) and CD45 (ab10558; Abcam Inc., Massachusetts, USA) SMSCs were induced to undergo adipogenic, chondrogenic, and osteogenic differentiation according to the manufacturer's instructions to characterize their pluripotency.

## 2.10 Biocompatibility

After 3 d of culture, the viability of SMSCs on the scaffolds was detected by Live/Dead staining. In detail, the scaffolds were immersed in 1 mL of a working solution containing 2 mmol/L calcein acetoxymethyl ester (AM) and 4 mmol/L ethidium homodimer-1 reagent, incubated for 1 h at room temperature, and the fluorescence intensity of calcein-AM or ethidium homodimer-1 was detected under a confocal microscope. SMSC survival on different scaffolds was detected by the Alamar Blue method (Thermo Scientific, USA) ($n$=5). Optical density (OD) values were then measured at 570 nm using a Varioskan Flash reader (Thermo Scientific; Waltham, Massachusetts, USA) [42]. To observe the morphology of SMSCs on the scaffolds, the scaffolds were fixed with 4% paraformaldehyde for 30 min at room temperature, stained with rhodamine-phosphatidylinositol-like protein (Cytoskeleton Inc., USA) for 1 h at 37 °C, and counterstained with Hoechst 33258 for 10 min.

## 2.11 Biochemical assays

To assess the fibrochondrogenic differentiation capacity of cells on the scaffolds, we incubated them in fibrochondrogenic medium containing α-MEM, connective tissue growth factor (CTGF, 100 ng/mL), and transforming growth factor-β3 (TGF-β3, 10 ng/mL). In detail [44], DNA, glycosaminoglycan (GAG), and collagen secretion were detected on Days 3 and 7. Then, the scaffolds were immersed in papain solution (125 mg/mL papain, 5 mmol/L ethylenediaminetetraacetic acid (EDTA), 100 mmol/L $Na_2HPO_4$, 5 mmol/L L-cysteine) for 16 h. DNA content was assessed by reacting 20 μL of treated samples with 200 μL of Hoechst 33258 working solution (2 μg/mL) for 1 h at 37 °C shielded from light. Then, 20 μL of the above-treated samples were reacted with 200 μL of 1,9-dimethylmethylene blue (DMMB) reagent for 30 min at room temperature, and the absorbance was measured at 525 nm. An enzyme-linked immunosorbent assay (ELISA) kit was used to determine the collagen content.

## 2.12 Gene expression analysis in vitro

Quantitative reverse transcription-polymerase chain reaction (RT-PCR) was performed to detect the gene expression of collagen I (*COL I*), collagen II (*COL II*), *SOX 9*, and aggrecan (*ACAN*) on Days 3 and 7 (Table S1 in the supplementary information). Briefly, RNA was extracted and reverse transcribed to cDNA using the TRIzol kit and cDNA reverse transcription kit (Thermo Fisher Scientific, USA). RT-PCR was performed as previously reported [45]. Target genes were quantified using the $\Delta\Delta C_t$ method.

## 2.13 Macrophage polarization on the scaffold

To assess the polarization response of macrophages on the scaffolds, RAW264.7 cells were incubated on SH and SH-Mg scaffolds for three days. Then, the gene expression of M2 markers (*Arg1*, *CD206*, and *IL-10*) and M1 markers (*Inos*, *Ccr7*, and *TNF-α*) (Table S2 in the supplementary information) was assessed using real-time quantitative polymerase chain reaction (qPCR) after 8 h of incubation with 100 ng/mL of lipopolysaccharide (LPS) in the culture medium [46]. In addition, Arg1 and Inos protein content was analyzed by immunofluorescence in the SH group and SH-Mg group. Rabbit anti-hepatic arginase polyclonal antibody (ab96183) was used to detect Arg1, and rabbit anti-Inos monoclonal antibody (ab209027) was used to detect Inos. Inos was then reacted with fluorophore-conjugated mouse IgG goat polyclonal secondary antibody (ab150113) against the primary antibody. Cell nuclei were co-stained using Hoechst 33258.

## 2.14 In vivo scaffold implantation

The surgery was performed according to our previous protocol [42]. All animals were 12-week-old New Zealand white rabbits with a body weight of 2.5 kg and randomized into four groups: a Blank group underwent meniscectomy only, an SH group underwent meniscectomy and SH scaffold implantation, an SH-Mg group underwent meniscectomy and SH-Mg scaffold implantation, and the Native group which did not undergo meniscectomy. After the animals were anesthetized and disinfected, the anterior medial parapatellar incision was selected to expose the medial meniscus. A medial meniscectomy was then performed, and a scaffold was implanted at the location of the meniscal defect. Then, the stent was sutured and fixed to the joint capsule at the edge of the meniscus and the incision closed layer by layer. To prevent infection, penicillin was used for 3 d postoperatively. At the corresponding time points, the animals were euthanized for retrieving samples.

## 2.15 Evaluation of regenerated meniscus

At the corresponding time points, grafts were sampled and photographed to investigate meniscus regeneration. The implant was fixed in paraformaldehyde, dehydrated, embedded in paraffin, and sectioned for histological staining including hematoxylin and eosin (HE), safranin O-fast green (SO), toluidine blue (TB), immunohistochemistry for collagen I and II, and picrosirius red (PSR).

The biomechanical characteristics of the regenerated meniscus were assessed at 12- and 24-week post-implantation. The compressive modulus of the SH group and SH-Mg group was established utilizing a Tri-boIndenter (Hysitron Corporation, USA), as previously described [47]. Tensile tests were conducted using a mechanical measuring instrument (AG-IS; Shimadzu), following established protocols [42].

## 2.16 Evaluation of cartilage protection

The International Cartilage Repair Society (ICRS) classification system was introduced to assess articular cartilage condition [48]. Cartilage samples were fixed, decalcified, embedded, and cut into paraffin sections. Finally, they were stained with HE, TB, and SO to grade using the Mankin score [49, 50].

## 2.17 Statistical analysis

All data are expressed as mean±standard deviation. Significance was determined by one-way analysis of variance (ANOVA) or Student's *t*-test. Statistical significance was determined as $p<0.05$.

## 3 Results and discussion

### 3.1 Rheological properties of hydrogels

The elastic and viscous modulus of the hydrogel flattened gradually with increasing angular frequency (Fig. 2b). In addition, the hydrogels exhibited significant shear-thinning characteristics, as evidenced by the clear reduction in viscosity with increasing shear rate (Fig. 2a). These findings suggested that hydrogels possess favorable printability.

### 3.2 Scaffold crosslinking

In this study, FTIR spectrometry was employed to assess potential crosslinks within the composite hydrogels. As illustrated in Fig. 2c, the peak at 1258 $cm^{-1}$ in the SF/HAMA and SF/HAMA-Mg groups was more pronounced than in the SF group. This peak corresponds to the C–N stretching vibration. Notably, the characteristic peaks of approximately 1655 $cm^{-1}$ were attributed to the α-form of SF. Furthermore, characteristic peaks in 1620–1635 $cm^{-1}$ and 1230–1235 $cm^{-1}$ indicated the presence of a β-sheet structure in SF. Further, the presence of distinct peaks at 1620 and 1517 $cm^{-1}$ signifies the tensile vibration of the carbonyl group (C=O) in the Amide I region and the deformation vibration of the nitrogen-hydrogen bond (N–H) in the Amide II region, respectively. These observations imply a change in the structure of SF from disordered coils to a more stable β-fold conformation. Thus, these findings evidence an interaction between SF and HAMA.

### 3.3 Scaffold microstructure

SEM images indicated that the SF scaffold had smaller pores than SF/HAMA and SF/HAMA-Mg (Fig. 2d). The pore size distribution analysis showed average diameters of 5.04, 8.58, and 13.47 μm for SF, SF/HAMA, and SF/HAMA-Mg hydrogels, respectively (Fig. 2e). The incorporation of HAMA and $Mg^{2+}$ resulted in increased pore size. However, hydrogels containing HAMA exhibited smaller porosity compared to the SF hydrogel, with the SF/HAMA-Mg hydrogel having the lowest porosity (Fig. 2f).

### 3.4 Biomechanical tests in vitro

To evaluate their biomechanical properties, we assessed the compressive and tensile strengths of the three scaffolds. The tensile moduli for the SF, SH, and SH-Mg scaffolds were (0.369±0.014), (0.376±0.011), and (0.408±0.024) MPa, respectively (Fig. 2g); the compressive moduli were (0.091± 0.009), (0.091±0.019), and (0.118±0.016) MPa, respectively (Fig. 2h). These findings suggest that the SH-Mg scaffold displayed better biomechanical characteristics than the other scaffolds, demonstrating superior performance in both compressive and tensile strength. This may be due to the addition of metal ions. The improved mechanical properties are crucial for withstanding stress in vivo in the scaffolds.

### 3.5 Degradation in vitro

The degradation rate of hydrogels was assessed in PBS and XIV solutions. Figure 2i shows that the SF group exhibited a comparatively lower degradation rate compared to the other two groups. This suggests that the incorporation of SF in the composite hydrogel had a mild decelerating effect on degradation. Thus, the SF group is more appropriate for achieving a harmonious equilibrium between scaffold degradation and the formation of neoplastic tissue.

### 3.6 Scaffold ESR

The composite hydrogel exhibited a lower ESR compared to the SF hydrogel (Fig. 2j). This decline in ESR was attributed to increased crosslinking density from the incorporation of HAMA and $Mg^{2+}$ into the hydrogel matrix. Despite an ESR of 101.77%, the SH/HAMA-Mg hydrogel demonstrated a remarkable ability to swiftly expand and absorb joint fluid, which was beneficial for buffering knee joint stress. Consequently, these hydrogels held promise for application in the repair of meniscus tissue.

### 3.7 $Mg^{2+}$ release rate

According to Fig. 2k, an initial surge of $Mg^{2+}$ ions was observed within the first week, followed by gradual deceleration over subsequent weeks. The rapid release in the early stage after implantation could effectively mitigate the local inflammatory response, while the later slow release could continue to play a role in a lower concentration for a longer period.

### 3.8 SMSC characterization

After the third passage, SMSCs displayed a fusiform shape and were evenly distributed following their expansion. To identify the multiple lineage differentiation capacities of SMSCs, a tri-lineage differentiation experiment was conducted. Mesenchymal stem cells (MSCs) could differentiate into three distinct cell lineages, namely adipocytes, osteocytes, and chondrocytes (Fig. 3a). Flow cytometry analysis revealed positive overexpression of the phenotypic markers CD44 and CD90, and negative expression of lipopolysaccharide receptor CD34 and leukocyte common antigen CD45 in SMSCs (Fig. 3b). After scaffold implantation into the site of meniscal injury, SMSCs in the knee joint migrated and adhered to the scaffold, proliferating and differentiating into fibrochondrocytes in response to the local microenvironment [51]. Previous research showed that SMSCs

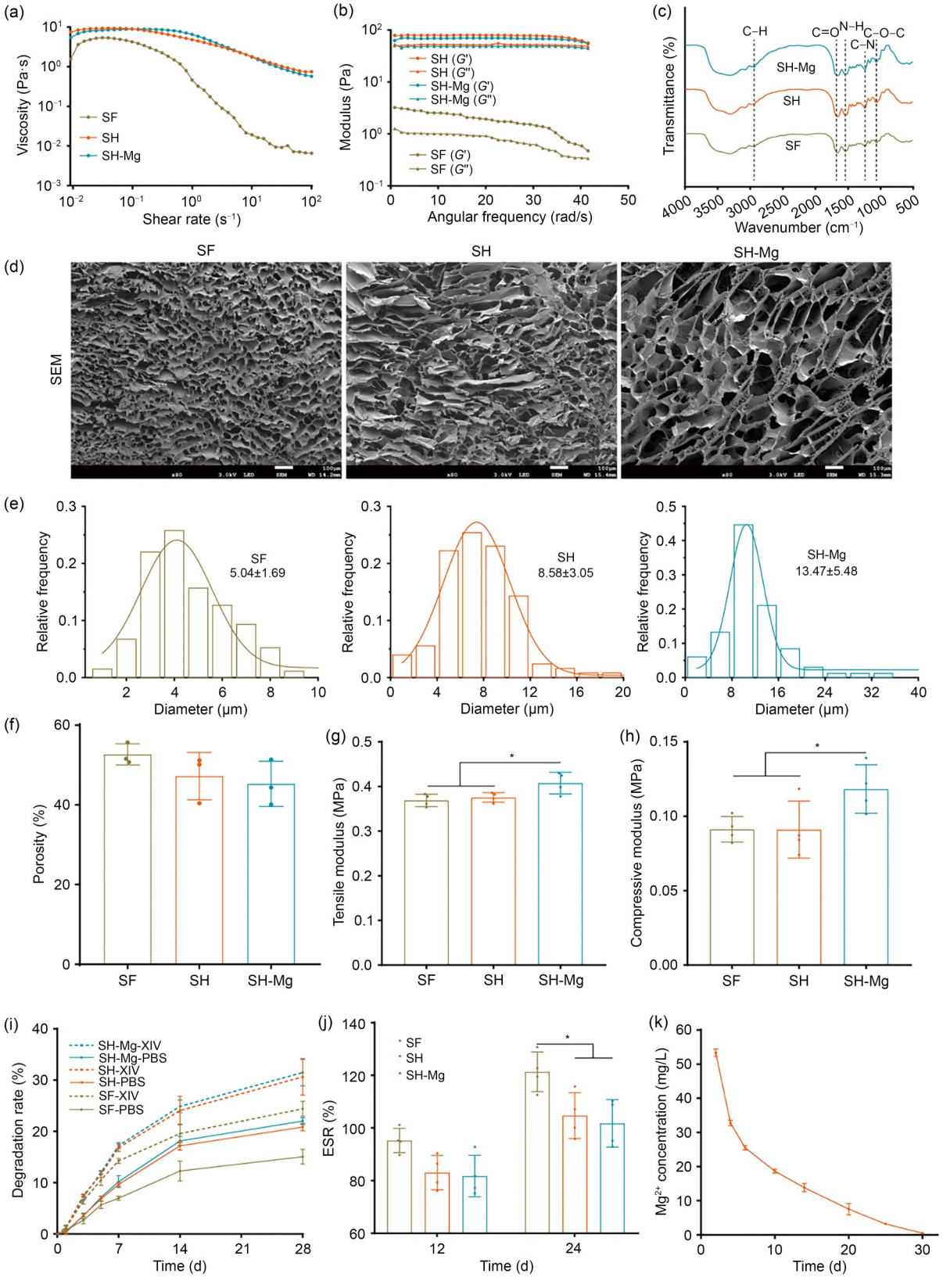


**Fig. 2** Scaffold characterization. Viscosity (a) and modulus (b) of SF, SH, and SH-Mg hydrogels. (c) FTIR spectra of SF, SH, and SH-Mg hydrogels. (d) Microstructure of SF, SH, and SH-Mg scaffolds after lyophilization (scale bar=100 μm). (e) Pore size distribution of SF, SH, and SH-Mg scaffolds. Porosity (f), tensile modulus (g), compressive modulus (h), degradation rate (i), ESR (j), and $Mg^{2+}$ release rate (k) of SF, SH, and SH-Mg scaffolds. Data are expressed as mean±standard deviation ($n$=4, $^{*}p<0.05$)

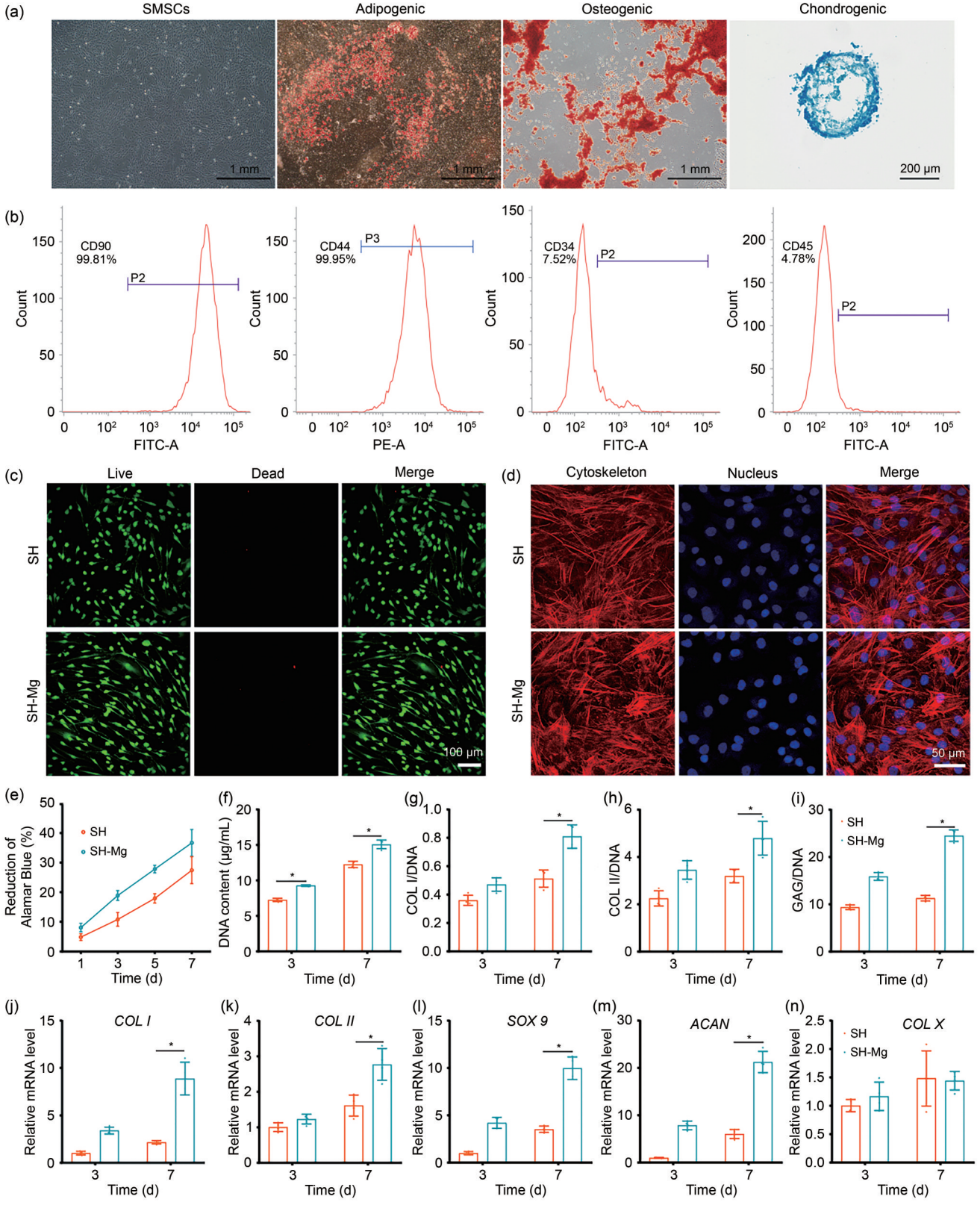


**Fig. 3** Biocompatibility of the scaffolds in vitro. (a) Adipogenic, osteogenic, and chondrogenic differentiation of SMSCs. (b) Flow cytometry analysis of SMSCs. Live/Dead staining (c) and Phalloidin/Hoechst assay (d) of SMSCs in the scaffolds. (e) Alamar Blue assay of SMSCs in the scaffolds. DNA (f), COL I (g), COL II (h), and GAG (i) of fibrocartilaginous matrix production. (j–m) Fibrocartilage-specific gene expression of *COL I* (j), *COL II* (k), *SOX 9* (l), and *ACAN* (m). (n) Gene expression of hypertrophy marker *COL X*. Data are expressed as mean±standard deviation ($n$=4, $^{*}p$<0.05)

are well suited for meniscal repair, with gene expression profiles similar to those of meniscal cells [51, 52].

### 3.9 Cell viability, adhesion, and proliferation of SMSCs on scaffolds

After three days of incubation on scaffolds, the Live/Dead assay demonstrated no substantial cell death on any scaffold, indicating that MSCs survived well on both the SH scaffold and the SH-Mg scaffold (Fig. 3c; Fig. S1 in the supplementary information). MSCs had a good stretching pattern on the scaffolds, indicating that the cells could attach to the scaffolds (Fig. 3d). Further, the Alamar Blue assay indicated a proliferative trend for SMSCs in both groups within 7 d (Fig. 3e). However, the proliferation rate in the SH-Mg group was higher than that in the SH group, which might be due to the addition of $Mg^{2+}$. These results indicated that the scaffolds had good biocompatibility.

### 3.10 ECM production in vitro

Similar to previous results, the DNA content in the SH-Mg group was significantly higher than that in the SH group (Fig. 3f). Both scaffolds could maintain cell activity and proliferation, while $Mg^{2+}$ encapsulation could further promote SMSC proliferation.

A DMMB assay was used to measure sulfated-glycosaminoglycan (sGAG) production by SMSCs. Figure 3 showed that the sGAG content on Day 7 was significantly higher than that on Day 3 in the SH-Mg group. Further, sGAG levels in the SH-Mg group were higher than in the SH group on Day 7, which revealed that SH-Mg scaffolds could better promote sGAG secretion (Fig. 3i). To confirm collagen production in both kinds of scaffolds, an ELISA assay was performed. The results of collagen secretion exhibited that COL I and COL II corrected by DNA increased over time, and SH-Mg scaffolds resulted in higher COL I and COL II deposition than the other (Figs. 3g and 3h). Overall, these results demonstrate that SH-Mg scaffolds promoted superior SMSC proliferation and meniscal matrix secretion compared with SH scaffolds.

### 3.11 Fibrochondrogenic differentiation of encapsulated SMSCs

Next, we investigated the expression of genes associated with fibrochondrogenic differentiation, such as the cartilaginous gene (*COL II*, *SOX 9*, and *ACAN*), fibroblast gene (*COL I*), and a cell hypertrophy marker (*COL X*). The relative mRNA level of *COL I* was markedly increased in the SH-Mg group compared to the SH group (Fig. 3j). At Day 3, *COL II* expression was similar between groups, but in hybrid scaffolds it was significantly higher at Day 7 (Fig. 3k). The expression level of *SOX 9* and *ACAN* was similar to that of *COL I* (Figs. 3l and 3m). Meanwhile, there was no significant change in the relative mRNA level of hypertrophy marker *COL X* over time in both scaffolds (Fig. 3n). These results indicate that the SH-Mg group has better potential for fibrochondrogenic differentiation.

### 3.12 SH-Mg hydrogel induced macrophage polarization toward the M2 phenotype

To simulate the inflammatory microenvironment and investigate the impact of $Mg^{2+}$ on macrophages within the SF/HAMA hydrogel, we used an LPS-RAW264.7 cell-SH-Mg hydrogel system. To detect macrophage polarization, RAW264.7 cells were cultured on both SH and SH-Mg hydrogels. Quantitative PCR analysis showed a significant decrease in the expression of *IL-6*, *Inos*, *Ccr7*, and *TNF-α* (M1 marker genes) in the SH-Mg hydrogel (Fig. 4a), while that of *Arg1*, *CD206*, and *IL-10* (M2 marker genes) significantly increased (Fig. 4b). Immunofluorescence analysis supported the aforementioned findings, evidencing a notable decrease in M1 markers (Inos) (Fig. 4c) and a substantial increase in M2 markers (Arg1; Fig. 4d) in the SH-Mg hydrogel.

$Mg^{2+}$ has been found to influence macrophage polarization throughout this process. RAW cells cultured using $Mg^{2+}$ hydrogel exhibited reduced expression of M1 genes and proteins, while showing increased expression of M2 genes and proteins. Moreover, the release of Arg1 by M2 macrophages is considered critical for supplying crucial building blocks for collagen and fibroblast activation factors in the context of the anti-inflammatory stage. In this study, immunofluorescence staining revealed a notable increase and sustained presence of M2 macrophages (Arg1), along with a decrease in M1 macrophages (Inos). These findings suggest that SH-Mg actively promotes M2 polarization during meniscus regeneration. In summary, a $Mg^{2+}$ hydrogel facilitates M1-to-M2 macrophage polarization, thereby serving as a valuable approach for biomaterial-guided meniscal tissue regeneration.

### 3.13 Meniscus regeneration

Meniscal regeneration was evaluated after the implantation of SH-Mg scaffolds into rabbits' knee joints. Imaging of the regenerated tissues in the different groups was assessed using magnetic resonance imaging (MRI) analysis (Fig. 5b). After 24 weeks, visible new menisci appeared in both SH and SH-Mg groups, with the regenerated tissue in the SH-Mg group closely resembling the morphology of the natural meniscus. In addition, the whole-organ magnetic resonance imaging score (WORMS) in the SH-Mg group was lower than that in other groups and closer

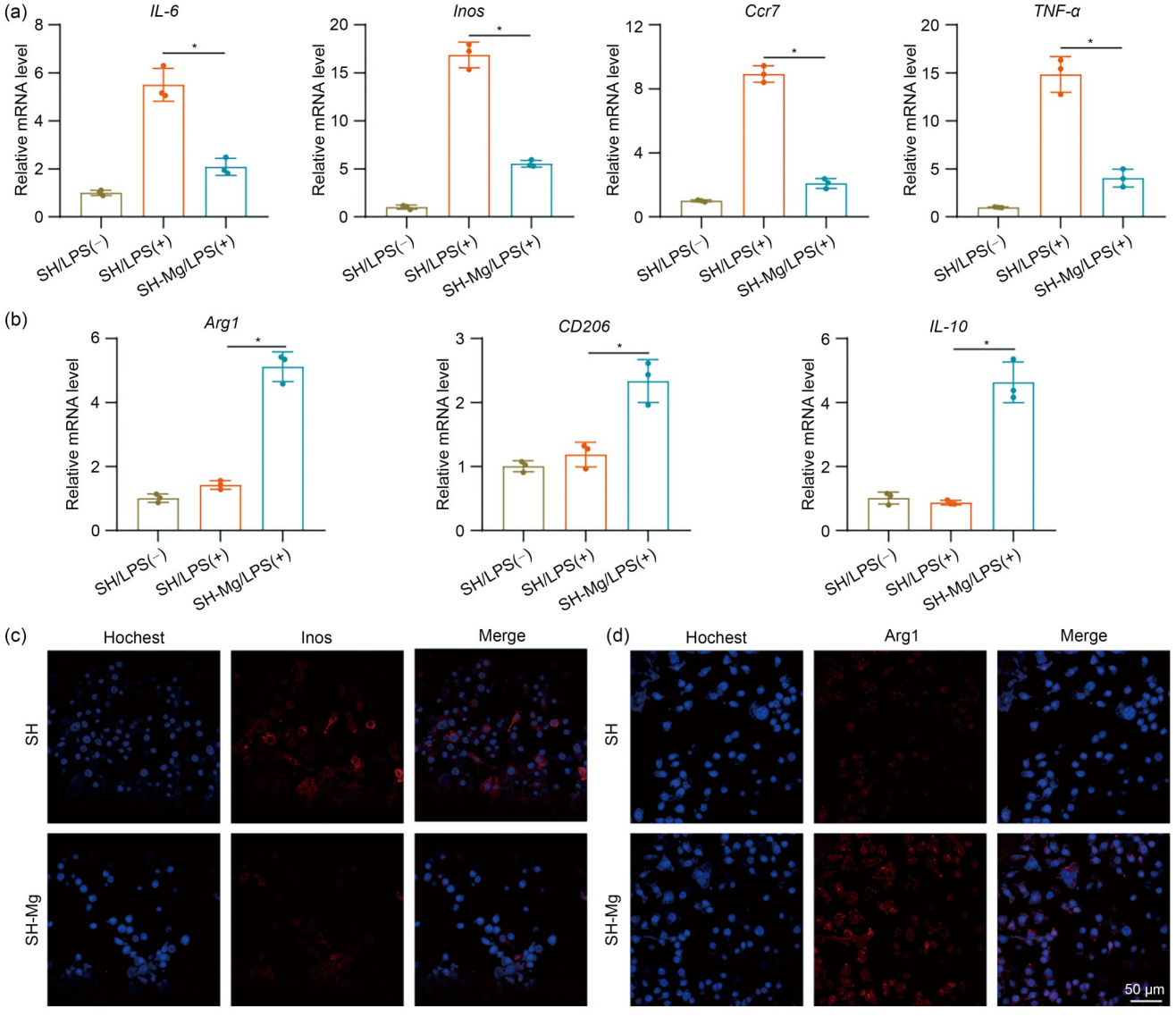


**Fig. 4** $Mg^{2+}$-contained scaffolds modulated macrophage polarization. (a) *IL-6*, *Inos*, *Ccr7*, and *TNF-α* (M1 marker genes). (b) *Arg1*, *CD206*, and *IL-10* (M2 marker genes) gene expression. Data are expressed as mean±standard deviation ($n$=3, $^{*}p$<0.05). (c) Immunofluorescence assessment of M1 markers (Inos protein). (d) Immunofluorescence analysis of M2 markers (Arg protein)

to the natural meniscus, highlighting the regenerative effect of the SH-Mg scaffold (Fig. 5e). Figure 5a shows the overall morphology of the regenerated meniscus, indicating that the SH-Mg group showed a more comprehensive and homogeneous regeneration of the meniscus at 24 weeks, along with improved joint integration.

Histological staining of the implants revealed a reduced foreign body reaction and fewer areas of cytopenia in the SH-Mg group compared to the SH group (Fig. 6a). Furthermore, PSR, TB, SO, and immunohistochemical stainings for collagen and proteoglycans were performed to evaluate the ECM content and distribution in the implants. PSR staining was significantly increased in COL I in the outer region of the implants in the SH-Mg group compared to the SH group at 24 weeks. This suggested an orderly collagen arrangement, in accordance with COL I immunohistochemistry. Meanwhile, SO and TB staining revealed similar results for proteoglycans, with the SH-Mg group exhibiting higher proteoglycan deposition compared to the SH group. The proteoglycans were predominantly located in the middle and inner zones of the implant, as observed in COL II immunohistochemistry. In addition, a semi-quantitative analysis of COL I (Fig. 6b) and COL II (Fig. 6c) was performed to assess collagen content. At 24 weeks post-implantation, the SH-Mg group demonstrated significantly higher IOD/area relative density of Col I in the outer zone and Col II in the inner zone compared to the SH group ($p$<0.05). This region-specific collagen deposition pattern closely mimicked the characteristic collagen distribution of native meniscus tissue. These results suggest that

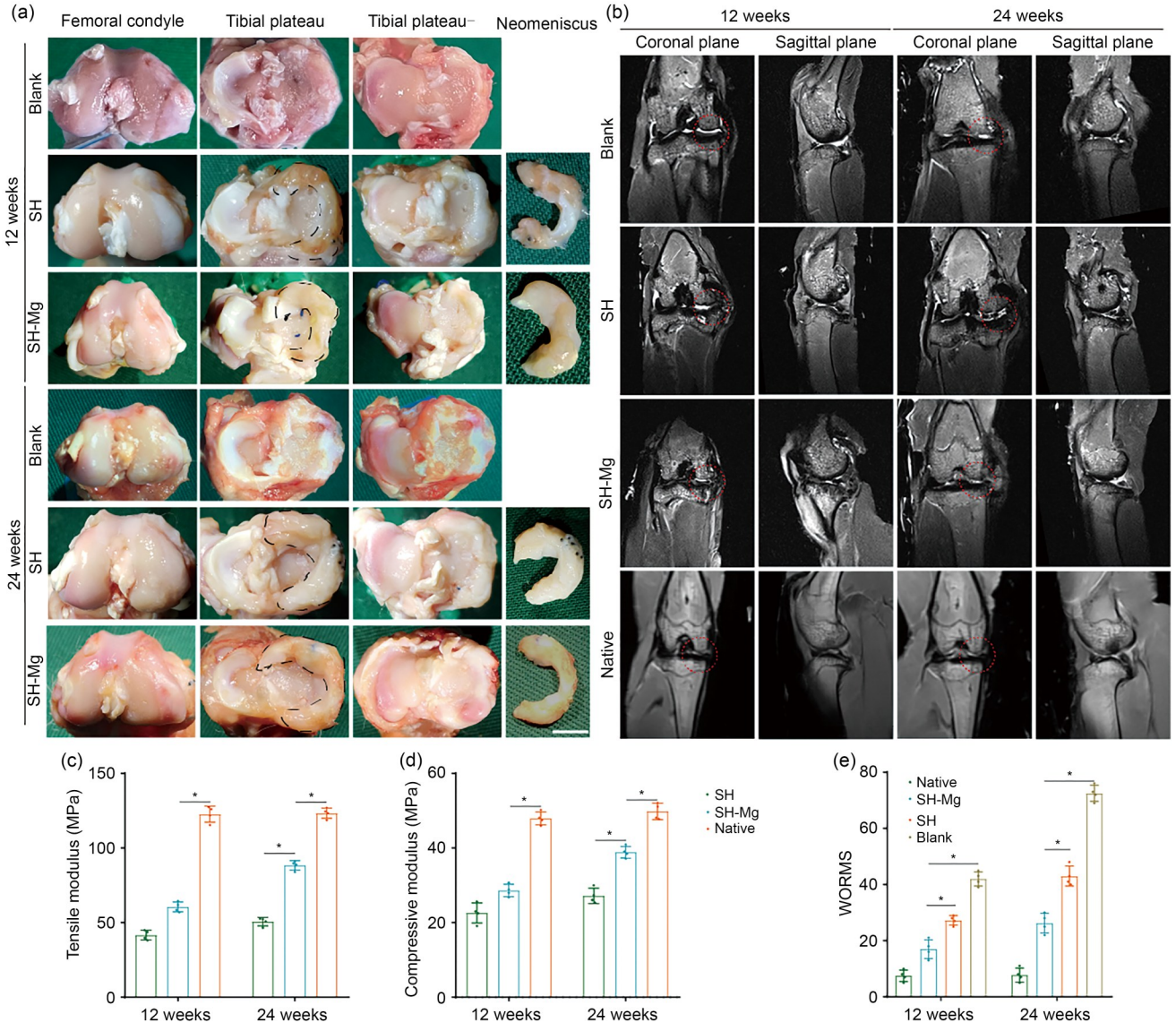


**Fig. 5** Macroscopic observation, MRI, and biomechanical evaluation of the regenerated meniscus in vivo. (a) Macroscopic observation of joints 12 and 24 weeks after implantation. The tibial plateau column represents the tibial plateau before removing the neoplastic meniscus (the dotted line marks the newly born medial meniscus), whereas the tibial plateau− column represents the tibial plateau after the neoplastic meniscus was removed (scale bar=10 mm). MRI of joints (b) and WORMS (e) 12 and 24 weeks after implantation. Tensile (c) and compressive (d) moduli of the regenerated meniscus in vivo. Data are expressed as mean±standard deviation ($n$=4, $^{*}p$<0.05)

$Mg^{2+}$-loaded scaffolds promote meniscal regeneration. ECM deposition is closely related to the role of regenerated tissues in stress loading and shock absorption in vivo.

The mechanical properties of the regenerated tissue are particularly important for meniscal repair; thus, we evaluated them at 12- and 24-week post-implantation. At 12 weeks, both SH and SH-Mg scaffolds exhibited inferior compressive and tensile moduli than the native meniscus. Conversely, at 24 weeks, the SH-Mg group displayed higher compressive and tensile moduli than the SH group, much closer to the native meniscus (Figs. 5c and 5d). Combined with the histological staining of the ECM, the SH-Mg group demonstrated more abundant deposition of collagen fibers and proteoglycans in the regenerated meniscus compared to the SH group, resulting in greater resistance to stretch and compression, improving mechanical performance in the knee joint.

## 3.14 Cartilage protection

It is essential to evaluate the protective effect of articular cartilage after implantation in vivo. Observing the overall cartilage performance (Fig. 5a) at 24 weeks, there was less cartilage degradation in the SH-Mg group than in the SH group. Histological analysis corroborated these findings (Fig. 7a). Further, the ICRS and Mankin scores indicated

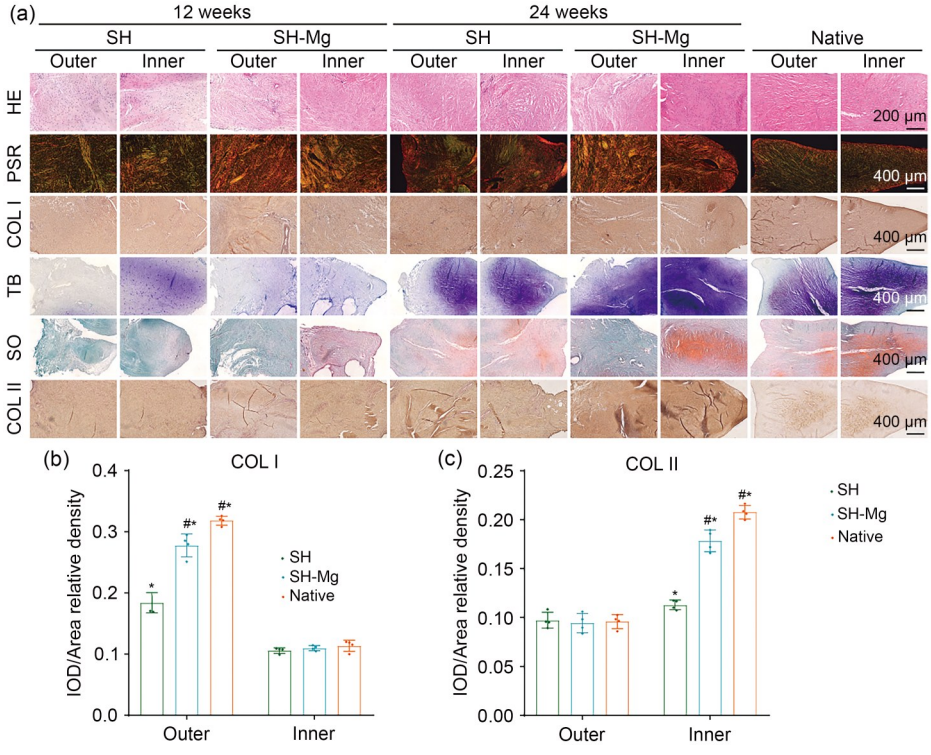


**Fig. 6** Histological evaluation of the regenerated meniscus in vivo. The outer column represents the synovial margin (outer region) of the meniscus, and the inner column represents the free edge (inner region) of the regenerated meniscus. (a) HE, PSR, TB, and SO staining, and immunohistochemical staining for COL I and COL II. (b, c) Immunohistochemical semiquantitative analyses of COL I and COL II (scale bar=200 μm in HE staining; scale bar=400 μm in PSR, TB, and SO staining, and immunohistochemical staining for COL I and COL II). Data are expressed as mean±standard deviation ($n$=4, $^{\#}p$<0.05 between the inner and outer regions in the same group, $^{*}p$<0.05 between the SH, SH-Mg, and Native groups in the same region)

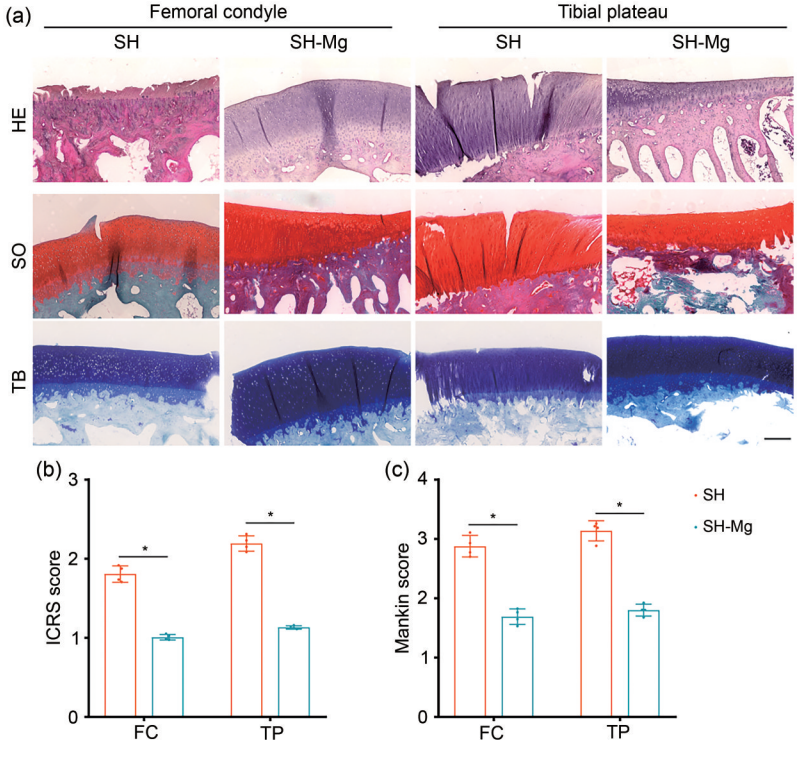


**Fig. 7** Cartilage histological assessment. (a) HE, SO, and TB staining of cartilage at 24 weeks (scale bar=200 μm). ICRS (b) and Mankin (c) scores. Data are expressed as mean±standard deviation ($n$=4, $^{*}p$<0.05)

that the SH-Mg group outperformed the SH group (Figs. 7b and 7c). These results suggested enhanced cartilage protection in the SH-Mg group, which was mainly due to the morphology, properties, and texture of regenerated meniscal tissues. It also showed higher cartilage protection in the SH-Mg group, with stress loading and shock absorption in vivo, thus demonstrating superior abilities. The limitation of our research was not conducted in large animal models. In the future, we will actively promote the application of magnesium ion composite scaffolds in large animal models and preclinical studies, as well as its important role in meniscal injury repair.

## 4 Conclusions

We successfully developed a composite hydrogel scaffold containing $Mg^{2+}$ with demonstrated beneficial cell proliferation, differentiation, and ECM generation. Moreover, the presence of $Mg^{2+}$ facilitated macrophage polarization from M1 to M2, significantly improving the local inflammatory environment. Consequently, the presence of $Mg^{2+}$ enhanced composite hydrogel scaffold, promoting meniscal regeneration and cartilage protection.

**Supplementary Information** The online version contains supplementary material available at https://doi.org/10.1631/bdm.2400313.

**Acknowledgements** This work was supported by grants from the Beijing Natural Science Foundation, China (No. 7244431), the Postdoctoral Science Foundation of China (No. 2022M710260), and the National Natural Science Foundation of China (No. 82202723).

**Author contributions** ZL: original draft, design, and manufacturing. WLS: original draft and conceptualization. MT: conceptualization. WQY and YFF: experimental assistance. JC and XQH: data collection and analysis. XG and YFA: supervision and writing—review & editing.

## Declarations

**Conflict of interest** The authors declare that they have no conflict of interest.

**Ethical approval** All animal use protocols were approved by the Experimental Animal Ethics Committee of Peking University Health Science Center (Approval No. PUIRB-LA2024020).

**Data availability** The data that support the findings of this study are available from the corresponding authors upon reasonable request.

## References

1. Fox AJS, Wanivenhaus F, Burge AJ et al (2015) The human meniscus: a review of anatomy, function, injury, and advances in treatment. Clin Anat 28(2):269–287. https://doi.org/10.1002/ca.22456
2. Makris EA, Hadidi P, Athanasiou KA (2011) The knee meniscus: structure-function, pathophysiology, current repair techniques, and prospects for regeneration. Biomaterials 32(30):7411–7431. https://doi.org/10.1016/j.biomaterials.2011.06.037
3. Zhan HW, Liu ZC, Wang YB et al (2023) Radiographic OA, bone marrow lesions, higher body mass index and medial meniscal root tears are significantly associated with medial meniscus extrusion with OA or medial meniscal tears: a systematic review and meta-analysis. Knee Surg Sports Traumatol Arthrosc 31(8):3420–3433. https://doi.org/10.1007/s00167-023-07418-8
4. Duong V, Oo WM, Ding CH et al (2023) Evaluation and treatment of knee pain: a review. JAMA 330(16):1568–1580. https://doi.org/10.1001/jama.2023.19675
5. Gee SM, Posner M (2021) Meniscus anatomy and basic science. Sports Med Arthrosc Rev 29(3):e18–e23. https://doi.org/10.1097/JSA.0000000000000327
6. Śmigielski R, Becker R, Zdanowicz U et al (2015) Medial meniscus anatomy—from basic science to treatment. Knee Surg Sports Traumatol Arthrosc 23(1):8–14. https://doi.org/10.1007/s00167-014-3476-5
7. Peng YC, Zhuang YL, Liu Y et al (2023) Bioinspired gradient scaffolds for osteochondral tissue engineering. Exploration 3(4): 20210043. https://doi.org/10.1002/EXP.20210043
8. Wan XY, Zhao YC, Li Z et al (2022) Emerging polymeric electrospun fibers: from structural diversity to application in flexible bioelectronics and tissue engineering. Exploration 2(1):20210029. https://doi.org/10.1002/EXP.20210029
9. Zhu TT, Jiang MY, Zhang MR et al (2022) Biofunctionalized composite scaffold to potentiate osteoconduction, angiogenesis, and favorable metabolic microenvironment for osteonecrosis therapy. Bioact Mater 9:446–460. https://doi.org/10.1016/j.bioactmat.2021.08.005
10. Schweizer C, Hanreich C, Tscholl PM et al (2023) Meniscal repair outcome in 3829 patients with a minimum follow-up from 2 years up to 5 years: a meta-analysis on the overall failure rate and factors influencing failure. Am J Sports Med 52(3):822–831. https://doi.org/10.1177/03635465231158385
11. Kopf S, Beaufils P, Hirschmann MT et al (2020) Management of traumatic meniscus tears: the 2019 ESSKA meniscus consensus. Knee Surg Sports Traumatol Arthrosc 28(4):1177–1194. https://doi.org/10.1007/s00167-020-05847-3
12. Eseonu KC, Neale J, Lyons A et al (2022) Are outcomes of acute meniscus root tear repair better than debridement or nonoperative management? A systematic review. Am J Sports Med 50(11):3130–3139. https://doi.org/10.1177/03635465211031250
13. Wang ZH, Le HX, Wang YB et al (2022) Instructive cartilage regeneration modalities with advanced therapeutic implantations under abnormal conditions. Bioact Mater 11:317–338. https://doi.org/10.1016/j.bioactmat.2021.10.002
14. Jin P, Liu L, Chen XC et al (2022) Applications and prospects of different functional hydrogels in meniscus repair. Front Bioeng Biotechnol 10:1082499. https://doi.org/10.3389/fbioe.2022.1082499
15. Resmi R, Parvathy J, John A et al (2020) Injectable self-crosslinking hydrogels for meniscal repair: a study with oxidized alginate and gelatin. Carbohydr Polym 234:115902. https://doi.org/10.1016/j.carbpol.2020.115902
16. Rothrauff BB, Sasaki H, Kihara S et al (2019) Point-of-care procedure for enhancement of meniscal healing in a goat model utilizing infrapatellar fat pad-derived stromal vascular fraction cells seeded in photocrosslinkable hydrogel. Am J Sports Med 47(14):3396–3405.

https://doi.org/10.1177/0363546519880468
17. Zhang Q, Xu ZY, Zhang XP et al (2022) 3D printed high-strength supramolecular polymer hydrogel-cushioned radially and circumferentially oriented meniscus substitute. Adv Funct Mater 32(23):13. https://doi.org/10.1002/adfm.202200360
18. Chen W, Li N, Ma Y et al (2019) Superstrong and tough hydrogel through physical cross-linking and molecular alignment. Biomacromolecules 20(12):4476–4484. https://doi.org/10.1021/acs.biomac.9b01223
19. Li Y, Fu RZ, Duan ZG et al (2022) Artificial nonenzymatic antioxidant MXene nanosheet-anchored injectable hydrogel as a mild photothermal-controlled oxygen release platform for diabetic wound healing. ACS Nano 16(5):7486–7502. https://doi.org/10.1021/acsnano.1c10575
20. Guo J, Shu XD, Deng H et al (2022) Stiff and tough hydrogels prepared through integration of ionic cross-linking and enzymatic mineralization. Acta Biomater 149:220–232. https://doi.org/10.1016/j.actbio.2022.06.008
21. Alketbi AS, Shi YF, Li HX et al (2021) Impact of PEGDA photopolymerization in micro-stereolithography on 3D printed hydrogel structure and swelling. Soft Matter 17(30):7188–7195. https://doi.org/10.1039/d1sm00483b
22. Bao YY (2022) Recent trends in advanced photoinitiators for vat photopolymerization 3D printing. Macromol Rapid Commun 43(14):e2200202. https://doi.org/10.1002/marc.202200202
23. Xu XY, Awad A, Robles-Martinez P et al (2021) Vat photopolymerization 3D printing for advanced drug delivery and medical device applications. J Contr Release 329:743–757. https://doi.org/10.1016/j.jconrel.2020.10.008
24. Lei T, Zhao YS, Zhai XR et al (2023) Photocurable hydrogel-elastomer hybrids as an adhesive patch for meniscus repair. Mater Des 229:111915. https://doi.org/10.1016/j.matdes.2023.111915
25. Hong H, Seo YB, Kim DY et al (2020) Digital light processing 3D printed silk fibroin hydrogel for cartilage tissue engineering. Biomaterials 232:119679. https://doi.org/10.1016/j.biomaterials.2019.119679
26. Singh M, Zhang JR, Bethel K et al (2021) Closed-loop controlled photopolymerization of hydrogels. ACS Appl Mater Interfaces 13(34):40365–40378. https://doi.org/10.1021/acsami.1c11779
27. Mendes BB, Daly AC, Reis RL et al (2021) Injectable hyaluronic acid and platelet lysate-derived granular hydrogels for biomedical applications. Acta Biomater 119:101–113. https://doi.org/10.1016/j.actbio.2020.10.040
28. Schuurmans CCL, Mihajlovic M, Hiemstra C et al (2021) Hyaluronic acid and chondroitin sulfate (meth)acrylate-based hydrogels for tissue engineering: synthesis, characteristics and preclinical evaluation. Biomaterials 268:120602. https://doi.org/10.1016/j.biomaterials.2020.120602
29. Shi W, Fang F, Kong YF et al (2021) Dynamic hyaluronic acid hydrogel with covalent linked gelatin as an anti-oxidative bioink for cartilage tissue engineering. Biofabrication 14(1):14107. https://doi.org/10.1088/1758-5090/ac42de
30. Noh I, Kim N, Tran HN et al (2019) 3D printable hyaluronic acid-based hydrogel for its potential application as a bioink in tissue engineering. Biomater Res 23(1):3. https://doi.org/10.1186/s40824-018-0152-8
31. Wang DZ, Guo YB, Zhu JC et al (2023) Hyaluronic acid methacrylate/pancreatic extracellular matrix as a potential 3D printing bioink for constructing islet organoids. Acta Biomater 165:86–101. https://doi.org/10.1016/j.actbio.2022.06.036
32. Peng ZW, Xue H, Liu X et al (2023) Tough, adhesive biomimetic hyaluronic acid methacryloyl hydrogels for effective wound healing. Front Bioeng Biotechnol 11:1222088. https://doi.org/10.3389/fbioe.2023.1222088
33. Jiang W, Hou FS, Gu Y et al (2022) Local bone metabolism balance regulation via double-adhesive hydrogel for fixing orthopedic implants. Bioact Mater 12:169–184. https://doi.org/10.1016/j.bioactmat.2021.10.017
34. Zhou ZY, Cui J, Wu SL et al (2022) Silk fibroin-based biomaterials for cartilage/osteochondral repair. Theranostics 12(11):5103–5124. https://doi.org/10.7150/thno.74548
35. Cengiz IF, Maia FR, da Silva Morais A et al (2020) Entrapped in cage (EiC) scaffolds of 3D-printed polycaprolactone and porous silk fibroin for meniscus tissue engineering. Biofabrication 12(2):025028. https://doi.org/10.1088/1758-5090/ab779f
36. Bandyopadhyay A, Mandal BB (2019) A three-dimensional printed silk-based biomimetic tri-layered meniscus for potential patient-specific implantation. Biofabrication 12(1):015003. https://doi.org/10.1088/1758-5090/ab40fa
37. Pan XH, Li R, Li WY et al (2024) Silk fibroin hydrogel adhesive enables sealed-tight reconstruction of meniscus tears. Nat Commun 15(1):2651. https://doi.org/10.1038/s41467-024-47029-6
38. Qiao W, Wong KHM, Shen J et al (2021) TRPM7 kinase-mediated immunomodulation in macrophage plays a central role in magnesium ion-induced bone regeneration. Nat Commun 12(1):2885. https://doi.org/10.1038/s41467-021-23005-2
39. Zhang XT, Huang PZ, Jiang GW et al (2021) A novel magnesium ion-incorporating dual-crosslinked hydrogel to improve bone scaffold-mediated osteogenesis and angiogenesis. Mater Sci Eng C Mater Biol Appl 121:111868. https://doi.org/10.1016/j.msec.2021.111868
40. Chen ZX Zhang W, Wang MY et al (2022) Effects of zinc, magnesium, and iron ions on bone tissue engineering. ACS Biomater Sci Eng 8(6):2321–2335. https://doi.org/10.1021/acsbiomaterials.2c00368
41. Yuan ZY, Wan Z, Gao CY et al (2022) Controlled magnesium ion delivery system for in situ bone tissue engineering. J Contr Release 350:360–376. https://doi.org/10.1016/j.jconrel.2022.08.036
42. Li Z, Wu NE, Cheng J et al (2020) Biomechanically, structurally and functionally meticulously tailored polycaprolactone/silk fibroin scaffold for meniscus regeneration. Theranostics 10(11):5090–5106. https://doi.org/10.7150/thno.44270
43. Moriguchi Y, Tateishi K, Ando W et al (2013) Repair of meniscal lesions using a scaffold-free tissue-engineered construct derived from allogenic synovial MSCs in a miniature swine model. Biomaterials 34(9):2185–2193. https://doi.org/10.1016/j.biomaterials.2012.11.039
44. Dai LH, He ZM, Zhang X et al (2014) One-step repair for cartilage defects in a rabbit model: a technique combining the perforated decalcified cortical-cancellous bone matrix scaffold with microfracture. Am J Sports Med 42(3):583–591. https://doi.org/10.1177/0363546513518415
45. Man ZT, Hu XQ, Liu ZL et al (2016) Transplantation of allogenic chondrocytes with chitosan hydrogel-demineralized bone matrix hybrid scaffold to repair rabbit cartilage injury. Biomaterials 108:157–167. https://doi.org/10.1016/j.biomaterials.2016.09.002
46. Jiang GY, Li SH, Yu K et al (2021) A 3D-printed PRP-GelMA

hydrogel promotes osteochondral regeneration through M2 macrophage polarization in a rabbit model. Acta Biomater 128:150–162. https://doi.org/10.1016/j.actbio.2021.04.010

47. Shi WL, Sun MY, Hu XQ et al (2017) Structurally and functionally optimized silk-fibroin-gelatin scaffold using 3D printing to repair cartilage injury in vitro and in vivo. Adv Mater 29(29):7. https://doi.org/10.1002/adma.201701089
48. Brittberg M, Winalski CS (2003) Evaluation of cartilage injuries and repair. J Bone Joint Surg Am 85(Suppl 2):58–69. https://doi.org/10.2106/00004623-200300002-00008
49. Wyatt LA, Moreton BJ, Mapp PI et al (2017) Histopathological subgroups in knee osteoarthritis. Osteoarthritis Cartilage 25(1): 14–22. https://doi.org/10.1016/j.joca.2016.09.021
50. Longo UG, Loppini M, Romeo G et al (2013) Histological scoring systems for tissue-engineered, ex vivo and degenerative meniscus. Knee Surg Sports Traumatol Arthrosc 21(7):1569–1576. https://doi.org/10.1007/s00167-012-2142-z
51. Hatsushika D, Muneta T, Nakamura T et al (2014) Repetitive allogeneic intraarticular injections of synovial mesenchymal stem cells promote meniscus regeneration in a porcine massive meniscus defect model. Osteoarthritis Cartilage 22(7):941–950. https://doi.org/10.1016/j.joca.2014.04.028
52. Ozeki N, Muneta T, Koga H et al (2013) Transplantation of Achilles tendon treated with bone morphogenetic protein 7 promotes meniscus regeneration in a rat model of massive meniscal defect. Arthritis Rheum 65(11):2876–2886. https://doi.org/10.1002/art.38099